In: 2023 AIAA Aviation and Aeronautics Forum and Exposition (AIAA AVIATION Forum), San Diego, 12-16 June 2023
Paper number AIAA 2023-4404; DOI:10.2514/6.2023-4404

Analysis of Triangular Cross-Section Slender Bodies in Supersonic Regime using RANS simulations

Quentin Bourny *, Anderson R. Proença †, Davide Di Pasquale ‡ and Simon A. Prince §
School of Aerospace, Transport, and Manufacturing, Cranfield University, Cranfield, United Kingdom, MK43 0AL

This paper presents an investigation on the ability of RANS simulations to capture the aerodynamic forces and the flow topology of triangular cross-section slender bodies. At Cranfield University's Transonic and Supersonic Wind Tunnel, force measurements and Schlieren images were obtained at zero incidence, Mach number equals to 2.5, and Reynolds number of $2.38 \cdot 10^5$ (based on section width). Tests were performed for three bodies of different nose geometries, but constant nose fineness ratio of 1.732. Tests were compared with RANS simulations for three turbulence models: Spalart-Allmaras, $k-\varepsilon$ Realizable and $k-\omega$ SST using the ANSYS Computational Fluid Dynamics software Fluent. In addition, simulations for a configuration presented in the literature which investigated several angles of attack were also conducted. At Mach 2.5, the normal force was predicted accurately by all turbulence models. The axial force, however, was clearly predicted more accurately with the $k-\varepsilon$ Realizable model. At the other hand, this turbulence model showed inferior ability to capture the flow features, particularly the leeside vortices. Spalart-Allmaras and $k-\omega$ SST gave similar results.

I. Nomenclature

C_A	=	Axial Force Coefficient
C_f	=	Friction Coefficient
C_N	=	Normal Force Coefficient
G	=	Growth Rate (for the prism layer)
l	=	Length of the body
l_c	=	Characteristic cell size
M_∞	=	Freestream Mach number
N	=	Number of layers (for the prism layer)
N_c	=	Number of cells in a mesh
P_∞	=	Freestream Static Pressure
r	=	Specific Gas Constant
Re_l	=	Reynolds number based on the length l
T_∞	=	Freestream Temperature
U_τ	=	Friction Velocity
$\mathcal{V}$	=	Volume of the computational domain
y_1	=	Height of the first cell of the prism layer
δ	=	Thickness of the boundary layer
γ	=	Heat Capacity Ratio
μ	=	Dynamic Viscosity
ρ	=	Air Density

II. Introduction

With the constant improvements of missiles and countermeasures, non-axisymmetric forebodies have gained momentum due to their aerodynamic performances. Several experimental studies showed triangular cross-section

*MSc Student, School of Aerospace and Transport Management, Cranfield University
†Lecturer in Aerodynamics, Centre for Aeronautics, AIAA Member
‡Lecturer in Aerodynamics, Centre for Aeronautics, AIAA Member
§Professor of Aerodynamics, Centre for Aeronautics, Senior AIAA Member

bodies provides higher levels of lift and lift-to-drag ratio compared with axisymmetric bodies [1–5].

However, considering the growing role played by Computational Fluid Dynamics in the design process, the use of RANS simulations for this kind of bodies is scarce in the literature and justifies the present study. The choice of the three turbulence models considered for the investigation was due to the widespread use of Spalart-Allmaras, $k-\varepsilon$, and $k-\omega$ models in industry. For the two latter class of models, a previous study showed $k-\varepsilon$ Realizable and $k-\omega$ SST had superior ability to predict accurately the aerodynamic forces in high-speed flows around a slender body [6].

This paper is composed of a review of the methodology used, including the geometry and the mesh dependency study. Then, it presents the results, and a conclusion summarizes the completed work and potential extensions.

III. Methodology

This investigation considered two sources of experimental data. The first one is from the NASA memorandum written by L. H. Jorgensen in 1958 entitled "Inclined bodies of various cross sections at supersonic speeds", performed at Mach 1.98 & 3.88 [1]. The second one consisted of a series of experiments performed at Mach 2.5 in the Supersonic and Transonic Wind Tunnel at Cranfield University, which are presented, for the first time, in this work. Herein, these two sources are referred as "Jorgensen" and "Cranfield" configurations.

A. Model Geometry

1. Cranfield Configuration

Three nose shapes had been considered in this study, as shown in Figure 1. All the models are not blunted. The tangent-ogive nose was built by extending the edges of the main body following a tangent-ogive curve. The faces were then created by straight connection between the edges. The pencil nose was built first by extending the edges following a tangent-ogive curve. A construction line was then defined connecting the centre of gravity of each cross-section. The main body faces were extended. In each cross-section plane, a circle was drawn connecting the extended edges and finally the nose was built extruding the superfluous material. It yielded to the aluminium models shown in Figure 2.

The body width measured 24.25 mm and the nose fineness ratio was 1.732. The cross-sectional area was equal to 255 mm^2.

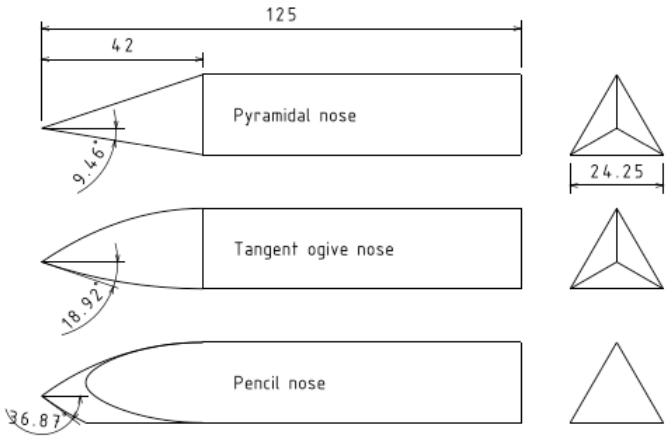

Fig. 1 Drawings representing the nose shapes considered in this study (all the lengths are in mm)

2. Jorgensen Configuration [1]

The model used by Jorgensen was a tangent-ogive, equilateral triangular cross-section model. The body width measured 47.95 mm and the nose fineness ratio was equal to 2.23. The whole model was 356 mm long.

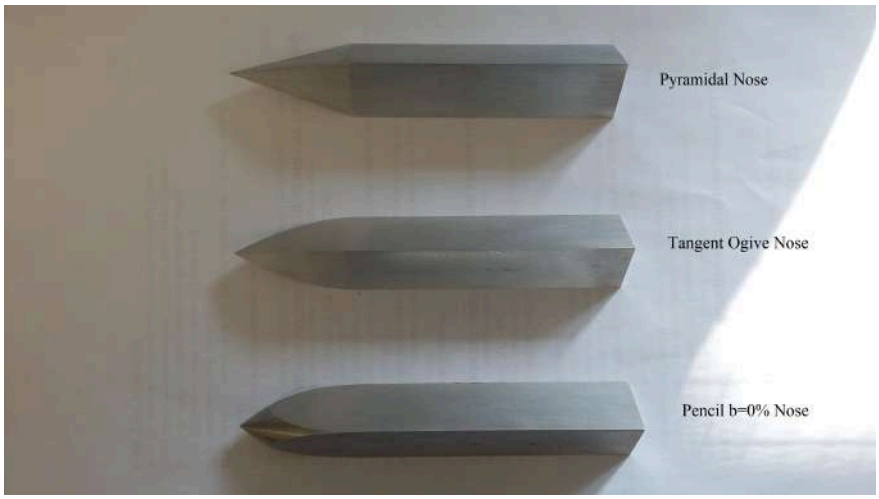

Fig. 2 Models manufactured for the wind tunnel measurements at Mach 2.5

B. Experimental Setup

1. Cranfield Configuration

Experiments were conducted in the Cranfield University Transonic/Supersonic Wind Tunnel, shown in figures 3a & 3b. This wind tunnel is a blowdown indraft tunnel. The axial and normal forces were measured using a 3-axis strain-gauge balance. Figure 4 shows the model mounted on the balance in the test section. The test section was a square with 63 mm of edge length. Transonic flows with a Mach number between 0.6 & 1.10 are produced with a unique transonic liner. For supersonic flows, several liners are available especially for Mach numbers 1.60 & 2.50, the former is displayed in Fig. 5. The tunnel was also equipped with a Schlieren imaging system. The base pressure was corrected a posteriori.

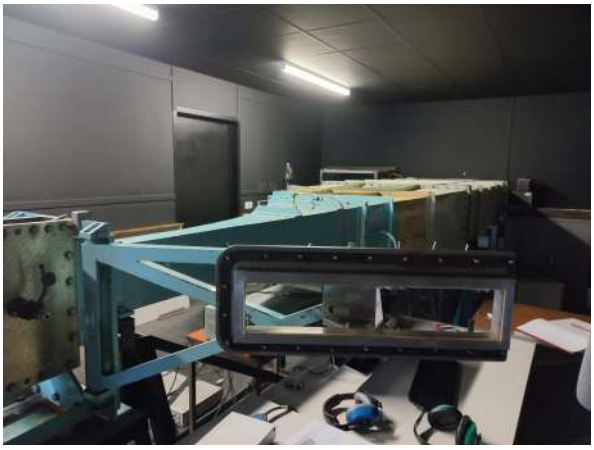

(a) Wind tunnel nozzle

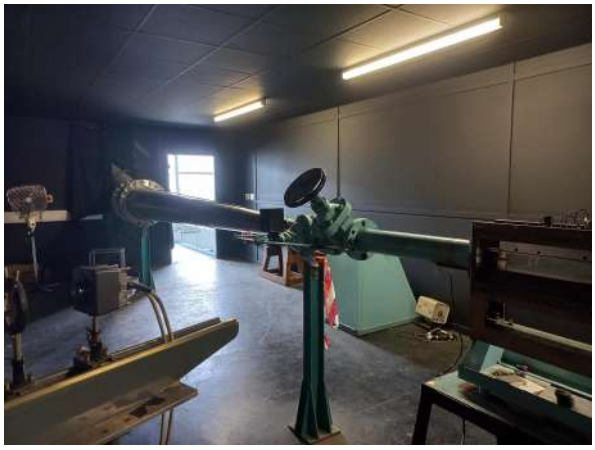

(b) Wind tunnel control valve

Fig. 3 Images of Cranfield University's Transonic/Supersonic Wind Tunnel

To obtain a turbulent boundary layer along the model location, transition was forced near the tip of the nose. Since the base pressure was not measured, the base drag was estimated based on CFD simulations of the exact geometry, i.e., with the exact geometry of the sting balance, and compared with literature data [7–12], which is publicly available for axisymmetric bodies.

Fig. 4 Pyramidal model mounted on the sting strain-gauge balance in the test section

Fig. 5 Wind Tunnel Working Section without a model and the Mach 1.6 Supersonic Liner

2. Jorgensen Configuration

The tests were conducted by Jorgensen in the Ames 1-ft by 3-ft supersonic wind tunnel number 1. A strain-gauge balance was present to measure the lift, drag and pitching moment. Orifices were located around the base periphery of the model to measure the base pressure. For additional details, the reader is referred to the original publication [1].

C. Flow Conditions

For the Cranfield configuration, the tests were performed for a Reynolds number based on the cross-section width of $2.38 \cdot 10^5$ and a Mach number of 2.5 at zero incidence. Assuming a Student's t-distribution, measurements were repeated seven times to guarantee an error due to repeatability inferior to 5%.

For the Jorgensen configuration, the Reynolds number was $6.7 \cdot 10^6$ based on the body length and the Mach numbers were 1.98 and 3.88. The range of angles of attack was 0° to 20° for Mach 1.98 and 0° to 15° for Mach 3.88. White-lead tests were performed at 10° and 14° angles of attack at Mach 1.98 and for 14° angle of attack at Mach 3.88. Water-vapour screen images were obtained at 5 and 10 reference lengths from the nose. The images at Mach 1.98 were acquired at the following angles of attack: 5°, 10°, 14° and 17°. At Mach 3.88, they were acquired at the following angles of attack: 5°, 10°and 14°.

D. Mesh Description

Flow phenomena associated with a triangular cross-section slender body moving at supersonic speeds are a pair of leeside vortices, shock waves, and rarefaction waves. Thus, the complex interplay of these phenomena leads to difficulties when creating a structured mesh adapted to the flow. For this reason, hybrid meshes were used in this work.

1. Height of the Prism Layer

To build the prism layer, three parameters are essential: the growth rate, G, the height of the first cell, y_1, and the number of layers, N. The growth rate is usually taken to be around 1.2, as to guarantee a smooth transition between each layer. For a given growth rate, the choice of N is equivalent to the choice of the overall thickness of the prism layer, δ, by the following relation:

$$\delta = y_1 \frac{G^N - 1}{G - 1}. \tag{1}$$

Thus, the overall thickness of the prism layer and the height of the first cell need to be estimated.

For a flat plate and a turbulent boundary layer after a length l measured from the plate's leading edge, the thickness can be calculated as,

$$\delta = \frac{0.37l}{Re_l^{0.2}}. \tag{2}$$

Using l as characteristic length scale, the Reynolds number based on the body length can be written as,

$$Re_l = \frac{P_\infty l M_\infty}{\mu}\sqrt{\frac{\gamma}{rT_\infty}}, \tag{3}$$

after using the perfect gas relation and the Mach number definition to substitute ρ and U_∞. Thus, the thickness is equal to:

$$\delta = \frac{0.37 l^{4/5} \mu^{1/5} (rT_\infty)^{1/10}}{(\sqrt{\gamma} P_\infty M_\infty)^{1/5}}. \tag{4}$$

The first cell height is given assuming a y^+ around the unity by the following relation:

$$y_1 = \frac{\mu}{\rho U_\tau}, \tag{5}$$

where U_τ is the friction velocity, equals to $\sqrt{\frac{1}{2} C_f \gamma r T_\infty M_\infty^2}$. After substituting the friction velocity, the height of the first cell is equal to:

$$y_1 = \frac{\mu\sqrt{2rT_\infty}}{P_\infty M_\infty \sqrt{\gamma C_f}}, \tag{6}$$

where C_f is the friction coefficient.

The friction coefficient for a turbulent compressible flow can be predicted using the following interpolation curve of Schlichting presented in [13]:

$$C_f = \frac{0.472}{(\log_{10} Re)^{2.58} \left(1 + \frac{\gamma - 1}{2} M_\infty^2\right)^{0.467}}. \tag{7}$$

In practice, the boundary layer obtained with the CFD is thicker than the estimated boundary layer. This result was expected, as the estimation is based on a flat plate profile while, in this project, the boundary layer is influenced by the pressure gradient induced by the geometry. It had been observed that thick prism layers of more than 1 mm and with a first cell height of 0.0015 mm gave the most suitable results in terms of convergence of the solution and compared to experiments.

2. Computational Domain

In Computational Fluid Dynamics, the chosen dimensions of the computational domain are fundamental to prevent an artificial forcing of the boundary conditions over the flow around the body of interest. The computational domain is shown in Figure 6. Relatively small angles of attack were considered to prevent the formation of axisymmetric vortices

around the body. For this reason, the flow is symmetric around the body, and thus, the domain was hemispherical. The domain is divided into three parts for the slender body: the nose, the forebody and the sting. All these surfaces are supposed to behave as walls for the flow. In Figure 6, the yellow surface is the outlet, the green one is named "farfield" and the blue one "inlet". The boundary condition for the "outlet" is set as pressure outlet and for two others as pressure far field. The pink surface corresponds to the symmetry plane of the body, and, thus, of the flow. In order to avoid interference between these surfaces and the body, the sting was taken two times longer than the whole body of interest, i.e., the union of the forebody and the nose, and the limits of the pressure far field boundaries is at 20 times the characteristic length.

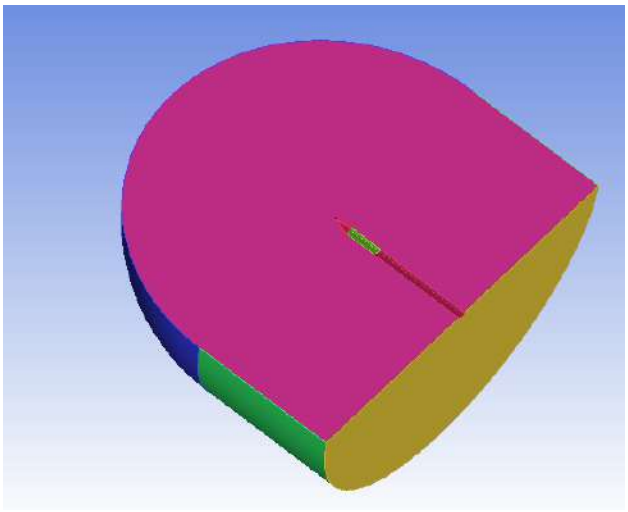

Fig. 6 Domain defined for the CFD simulations

A density box was created around the body to obtain better results without thinly refining the regions where globally the conditions are similar to the boundaries. On ICEM, an unstructured mesh was at first generated using the Octree method and afterwards the prism layer was generated using the Pre-inflation method "Fluent Meshing". Figure 7 illustrates the mesh obtained for the pencil nose geometry in the symmetry plane.

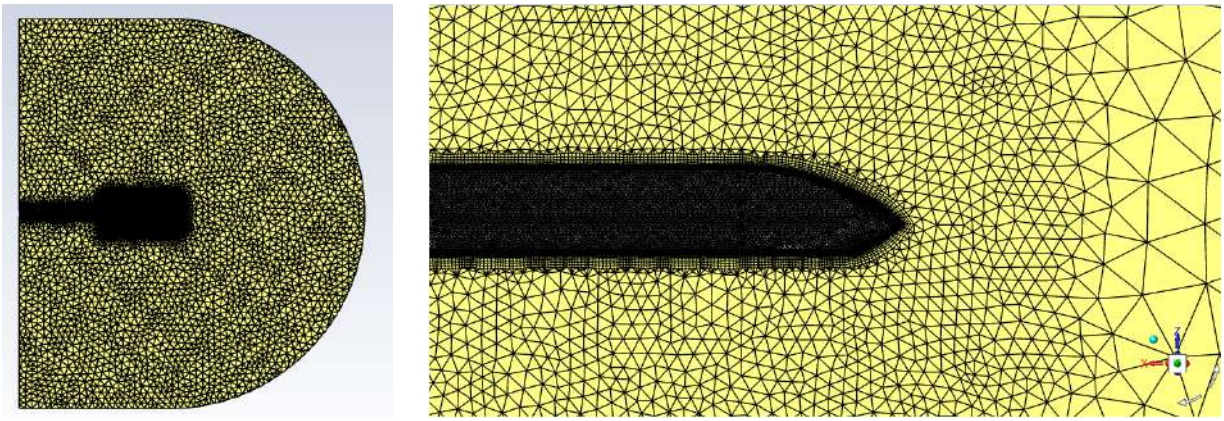

(a) Full-domain mesh in the symmetry plane **(b) Mesh around the nose in the symmetry plane**

Fig. 7 Sample mesh generated in the work

All modified parameters used to build the meshes used for the simulations are summarized in tables 1 and 2. Table 1 gives the element sizes in every part of the mesh, while Tab. 2 summarizes the parameters used to define the density box and the prism layer.

For the computations of the forces, the meshes described before are directly used, whereas, in the case of comparison with flow visualizations, the mesh is refined. The refinements are described in the Table 3.

Situation	Cranfield Pencil nose	Cranfield Pyramidal nose	Cranfield Tangent-ogive nose	Jorgensen's work
Maximal element size (overall)	40	40	30	70
Maximal element size (nose)	1	1	1	1
Maximal element size (forebody)	1	1	1	2
Maximal element size (sting)	2	2	2	5
Maximal element size (symmetry & outlet)	30	40	30	70
Maximal element size (farfield & inlet)	40	40	30	70

Table 1 Key Parameters used for the meshes (all lengths in mm)

Situation	Cranfield Pencil nose	Cranfield Pyramidal nose	Cranfield Tangent-ogive nose	Jorgensen's work
X-Coordinates Density Box	$-20 \leq X \leq 160$	$-20 \leq X \leq 160$	$-20 \leq X \leq 160$	$-80 \leq X \leq 300$
Y-Coordinates Density Box	$-60 \leq Y \leq 0$	$-60 \leq Y \leq 0$	$-60 \leq Y \leq 0$	$-40 \leq Y \leq 40$
Z-Coordinates Density Box	$-40 \leq Z \leq 40$	$-40 \leq Z \leq 40$	$-40 \leq Z \leq 40$	$0 \leq Z \leq 30$
Maximal element size (density box)	5	5	6	4
Prism layer: initial height	0.0015	0.0015	0.0015	0.0015
Prism layer: height ratio	1.2	1.2	1.2	1.2
Prism layer: number of layers	33	33	33	33
Prism layer: total height	3.0689	3.0689	3.0689	3.0689
Total number of cells	1006567	1050411	1147230	1026497

Table 2 Prism Layers and Density Box Parameters used for the meshes (all lengths in mm)

E. Mesh Dependency Study

In order to ensure grid convergence, several meshes were generated in this study. Details regarding these meshes are presented in tables 4, 5 & 6. The characteristic cell size l_c is calculated using the following equation,

$$l_c = \left(\frac{\mathcal{V}}{N_c}\right)^{1/3}. \tag{8}$$

Experimentally, the relative uncertainty on the axial force coefficient was observed to be superior or equal to 10^{-2}.

Parameters	Cranfield models at Mach 2.5	Jorgensen's model at Mach 1.98	Jorgensen's model at Mach 3.88
Refinement criterion	Static pressure outside range between 5840 Pascal and 5844 Pascal	Mach number above 1.983	Mach number above 3.881
Level of refinement	1	4	4

Table 3 Summary of the main features used for the mesh refinements

Number of cells	939413	1183371	2081272	4075029	9518802
Characteristic cell size (mm)	8.2	7.6	6.3	5.0	3.8
Relative difference in C_A with the finest grid ($\times 10^{-3}$)	2.1	3.9	0.45	-2.6	0

Table 4 Characteristics & Comparative Results for the pencil nose configuration

Number of cells	645538	859432	1677064	2442086	4100690	7482161
Characteristic cell size (mm)	9.3	8.4	6.7	5.9	5.0	4.1
Relative difference in C_A with the finest grid ($\times 10^{-3}$)	-12.6	1.4	7.2	0.46	-0.64	0

Table 5 Characteristics & Comparative Results for the pyramidal nose configuration

Number of cells	596562	954141	1631534	2311003	4098124	6487089
Characteristic cell size (mm)	9.5	8.1	6.8	6.1	5.0	4.3
Relative difference in C_A with the finest grid ($\times 10^{-3}$)	11.9	6.1	4.1	6.7	4.1	0

Table 6 Characteristics & Comparative Results for the tangent-ogive nose configuration

Thus, the error due to the spatial discretization was negligible for meshes with more than 900, 000 cells. The coarser mesh, satisfying this condition was selected for each configuration or nose geometry considered.

F. Simulation Setup

Since the flow presents shock waves but is not time-dependent, steady compressibility effects shall be accounted. For this reason, the solver is density-based and steady. The air is assumed to behave as an ideal gas with a specific heat constant of 1006.43 J/kg.K, a thermal conductivity constant of 0.0242 W/m.K and a molecular weight constant of 28.966 kg/kmol, while the viscosity follows the Sutherland's law.

The boundary conditions are based on the freestream values summarized in Table 7, together with the reference area and length. The turbulent intensity is set to 1% and the turbulent viscosity ratio is set to 10. These choices are based on previous unpublished experiments conducted at Cranfield University's Transonic/Supersonic Wind Tunnel.

The solver formulation is explicit with AUSM flux, least squares cell based gradient, third-order MUSCL flow discretization and second order upwind for the discretization of the turbulent parameters. The Courant number is chosen equal to 0.5 and the under-relaxation factors are set to the default values: 0.8 for the turbulent kinetic energy and the turbulent dissipation rate and equal to 1 for the remaining factors.

The standard initialization was used with "farfield" conditions. For the Cranfield configuration, 15,000 iterations were performed, whilst 20,000 iterations were performed for the Jorgensen configuration. For the refined meshes, 20,000 additional iterations were systematically performed.

Parameter	Cranfield's model at Mach 2.5	Jorgensen's model
Reference length (mm)	24.25	34.214
Reference area (cm^2)	2.5462	2.534
Freestream Mach number(s)	2.5	1.98 & 3.88
Freestream static pressure (in Pascal)	5841.1	27344.5 & 4136.564
Freestream temperature (in Kelvin)	130.2222	164.3144 & 73.0887

Table 7 Conditions used for the simulations

IV. Results and Discussion

The force measurements and Schlieren images obtained in the University of Cranfield raised several assumptions about the physical reasons which could explain the differences between experimental and simulated data, and among the turbulence models. In order to validate these assumptions or at least further investigate them, an additional configuration from the literature was numerically studied and compared with the published experimental results. For this reason, this section starts with the results obtained for the Cranfield configuration.

A. Cranfield Configuration

Figure 8 shows the axial force coefficient measured for the three nose shapes investigated. The experimental uncertainty is indicated at the top of each bar, and it includes the error due to the estimation of the base drag. The pencil nose produces almost twice as much axial force than the other two configurations, which in turn produce similar axial force coefficients.

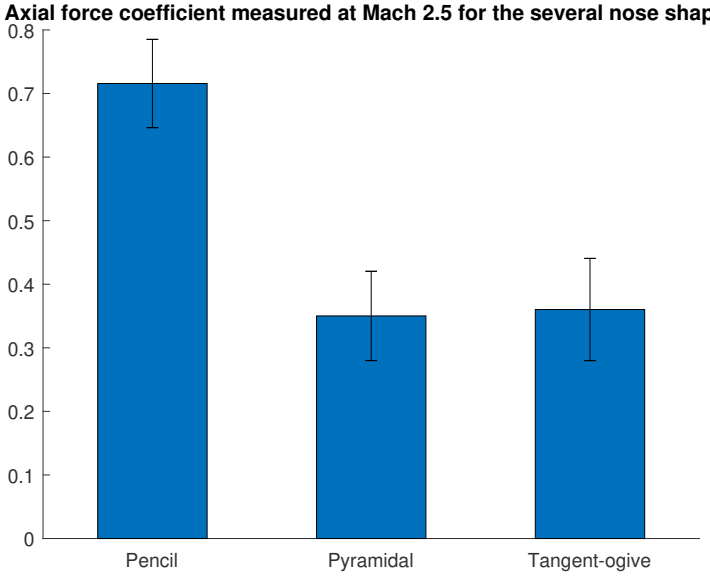

Fig. 8 Axial Force Coefficient at Mach 2.5 measured for the several nose shapes

Figure 9 presents the axial force coefficients measured and predicted by each turbulence models. The measured axial force coefficient is equivalent for the pyramidal and tangent-ogive nose shapes but approximately twice larger for the pencil nose shape. For all the nose shapes, the measured axial force coefficient is superior to the numerically-predicted ones. The axial force coefficient predicted with CFD is superior for the $k-\varepsilon$ Realizable turbulence model than for the two other turbulence models. This observation is still valid for the normal force coefficient. As shown in figures 9a, 9b & 9c, the axial force coefficient obtained with the $k-\varepsilon$ Realizable turbulence model is consistently closer to the lower bound of the uncertainty interval for the measured value. Considering the error due to the base pressure correction and

the uncertainty due to the freestream conditions, it is difficult to conclude how close the CFD predictions of the axial force are from the real value. However, it could be assumed the uncertainty interval defined as previously includes the actual value of the drag. If it is true, the comparison of the turbulence models would still show a superiority of the $k-\varepsilon$ Realizable model to capture the axial force.

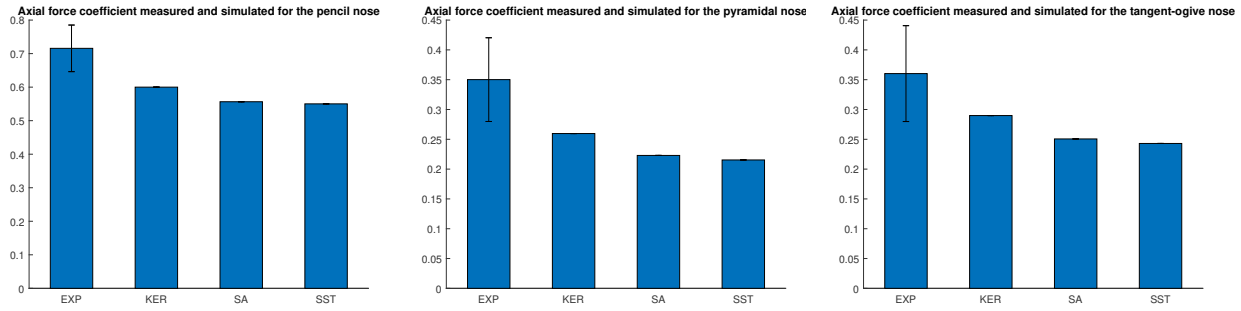

(a) pencil nose shape **(b) pyramidal nose shape** **(c) tangent-ogive nose shape**

Fig. 9 Axial Force Coefficient at Mach 2.5 measured and predicted with the three selected turbulence models

In terms of normal force, the measured value before correction is close to zero and since the precision of the balance is unknown, the uncertainty on the normal force coefficient is important. However, the predicted value does not significantly vary with the turbulence models and holds in the confidence interval, as shown in figures 10a, 10b & 10c.

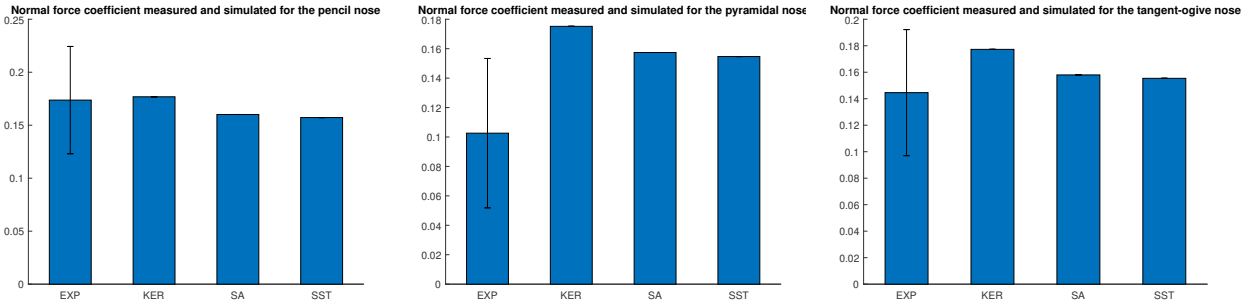

(a) pencil nose shape **(b) pyramidal nose shape** **(c) tangent-ogive nose shape**

Fig. 10 Normal Force Coefficient at Mach 2.5 measured and predicted with the three selected turbulence models

For the axial force, a more detailed comparison between the turbulence models can be achieved since the viscous and pressure components are computed. Figure 11 shows the division between the two components for each nose shape. For the pencil nose, the main contributor is surely the pressure component representing approximately 75% of the total axial force whereas for the other two nose shapes, the contribution of each component is approximately equal. It should indicate the shock waves are different between the pencil nose which should exhibit a curved conical shock causing a superior drag penalty than the straight conical shock for the two other nose shapes. In order to validate this assumption, Schlieren images and density contours were acquired to compare the flow features and more specifically the shock wave at the nose.

To understand with more details the observed difference in terms of axial force between the turbulence models, Figures 12a & 12b compare respectively the pressure & viscous components between each turbulence model and for all the nose shapes. The pressure component barely varies between the turbulence models. Contrary to the pressure component, the viscous component obtained with $k-\varepsilon$ realizable model is approximately 30% higher than the one obtained with $k-\omega$ SST model. The viscous component obtained with Spalart-Allmaras model is slightly superior to the predictions by the $k-\omega$ SST model.

At Mach 2.5, for each nose shape, Schlieren images were captured to identify the main flow features and compare them with the CFD results. Since Schlieren images are obtained through interference induced by the variation of density,

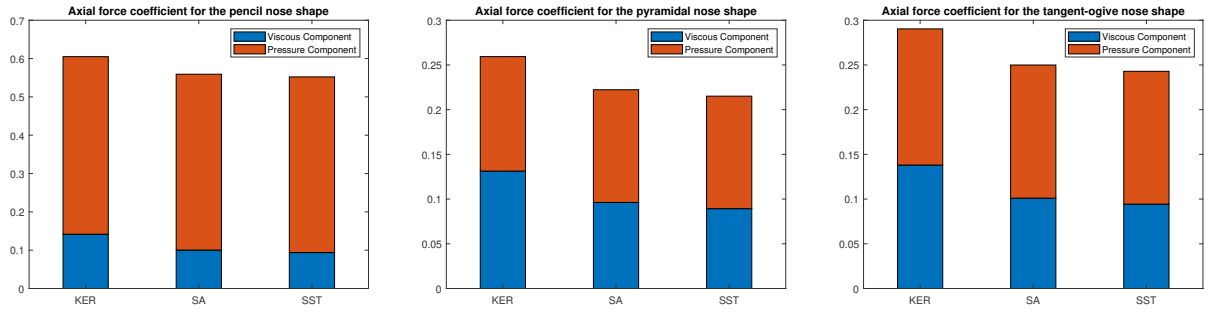

(a) pencil nose shape **(b) pyramidal nose shape** **(c) tangent-ogive nose shape**

Fig. 11 Axial force coefficient divided by viscous and pressure components for each turbulence model

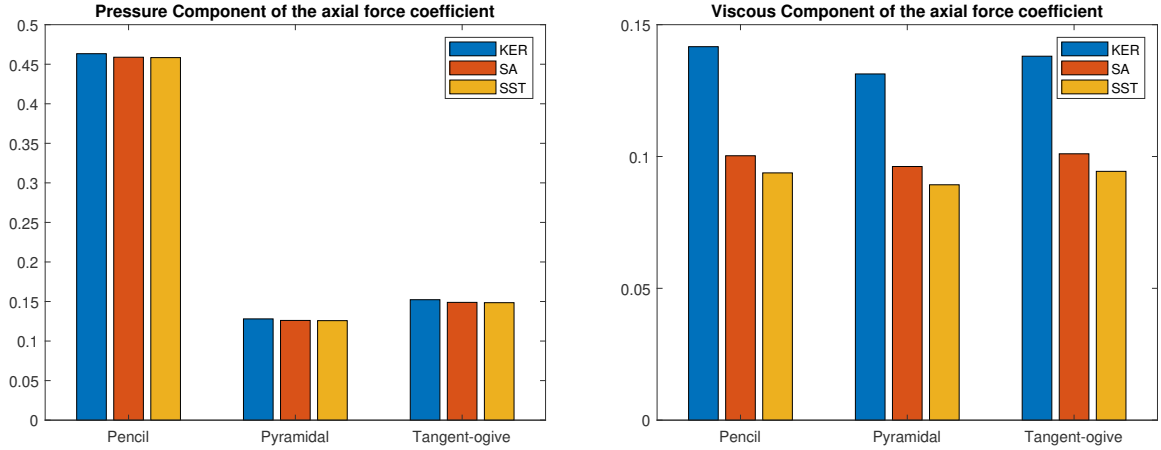

(a) Pressure Component **(b) Viscous Component**

Fig. 12 Viscous and Pressure components of the axial force coefficient divided by nose shapes and turbulence model

the Schlieren images are compared with density contours. The contours were created at the symmetry plane. Figure 13 displays the comparison between the Schlieren images and the CFD results.

For the pencil nose shape, in Figure 13a, an attached bow shock occurs at the nose of the model. A light region in the Schlieren image is located at the higher edge and is curved. It could indicate a lowdensity region, probably due to a rarefaction wave followed by a weak compression wave. These features are all captured by CFD and positioned correctly. The height of boundary layer at the upper edge is qualitatively similar between the CFD results and the Schlieren image where the boundary layer appears in white.

For the pyramidal nose shape, in Figure 13b, an attached oblique shock is located at the nose. An expansion fan is observed at the lower face of the body due to the transition between the nose and the main body. An expansion occurs at the upper edge but it is spatially restricted and thus, not as visible as the expansion fan at the lower face. The density contour for every studied turbulence model matches with the Schlieren image.

For the tangent-ogive nose shape, in Figure 13c, only an oblique shock is observed, and this is also captured by CFD. A low density zone downstream of the shock, near the main body, is indicated by in lighter grey on the upper edge, and respectively in darker colour on the lower face, and this zone is captured by CFD.

Overall, the flow physics is consistent between the different turbulence models and the experiments. The kind of shock observed at the nose is consistent with the observed difference in terms of pressure drag presented in Figure 12a. The curved conical shock observed for the pencil nose, whereas the other two nose shapes cause a straight conical shock, involves a larger drag penalty and is the main explanation of the drag penalty for this nose shape compared to the

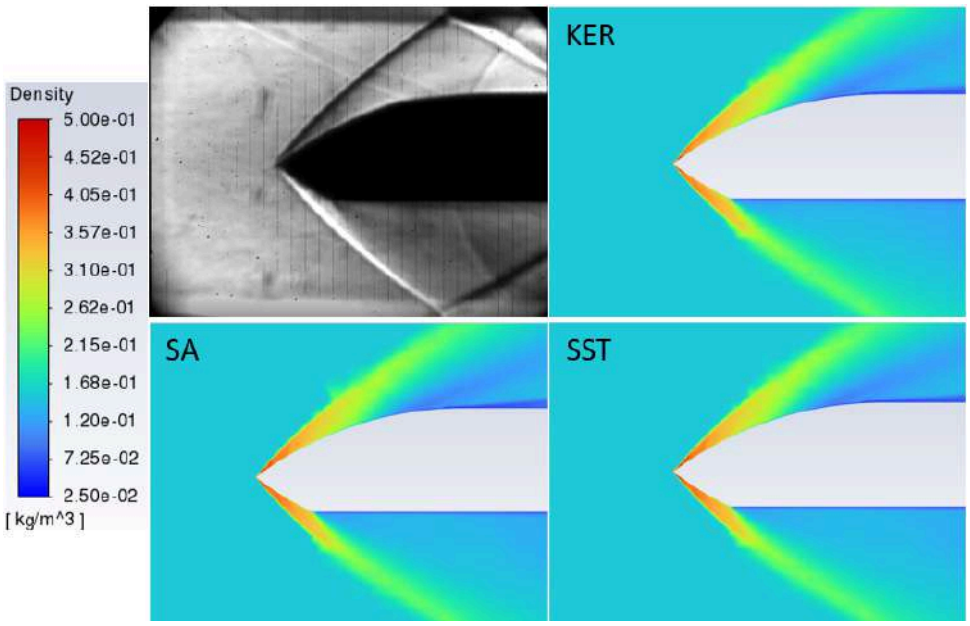

(a) pencil nose shape

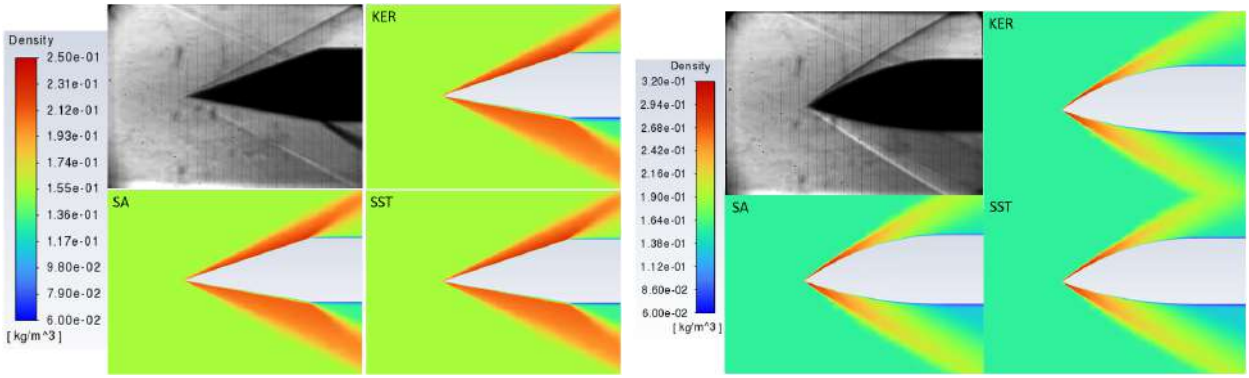

(b) pyramidal nose shape **(c) tangent-ogive nose shape**

Fig. 13 Comparison between the Schlieren image of flow and density contours at the symmetry plane for $k-\varepsilon$ Realizable, Spalart-Allmaras and $k-\omega$ SST turbulence models at Mach 2.5

tangent-ogive and pyramidal noses. The main difference between the results for each turbulence model holds in the height of the boundary layer, which is observed thicker for $k-\varepsilon$ Realizable model at the lower face in Figures 13b & 13c. This difference is consistent with the results concerning the drag coefficient where it was observed the $k-\varepsilon$ Realizable model predicts the viscous drag 30% higher than the $k-\omega$ SST model and which predicts slightly inferior values than the Spalart-Allmaras model.

In order to understand the difference observed between the turbulence models in terms of viscous drag, Mach number profiles were extracted in the symmetry plane on the lower face every 1 cm between 2 and 8 cm from the nose. The profiles for each turbulence model and nose shape are shown in Figures 14 to 20. All these figures show, qualitatively-speaking, a similar evolution of the boundary layer, independently of the chosen turbulence model. This result explains the relatively constant contribution of the nose and main body in terms of viscous drag described previously.

Figures 14, 15a & 15b, obtained for the pencil nose shape, shows that all the profiles converge to the same Mach number. This is a consequence of the geometry as observed in Figure 13a. The geometry of the faces causes constant flow conditions in the symmetry plane for all the considered conditions. This constant flow is due to the shock wave which is kept close to the nose curvature and since the nose ends with a steep transition to the main body, the geometrical transition limits the interaction with the shock and prevent the formation of an expansion fan.

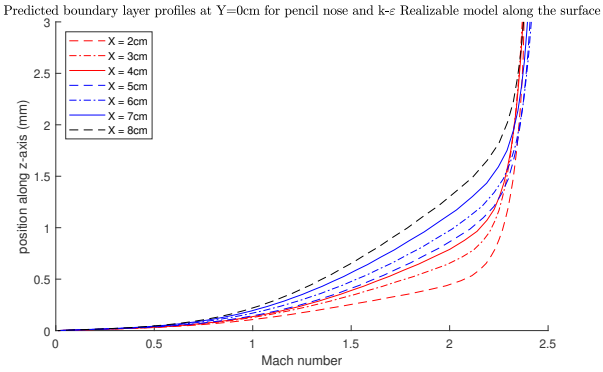

Fig. 14 Boundary Layer Profiles along the body at the intersection of the lower face and symmetry plane for the pencil nose and $k-\varepsilon$ Realizable turbulence model at Mach 2.5

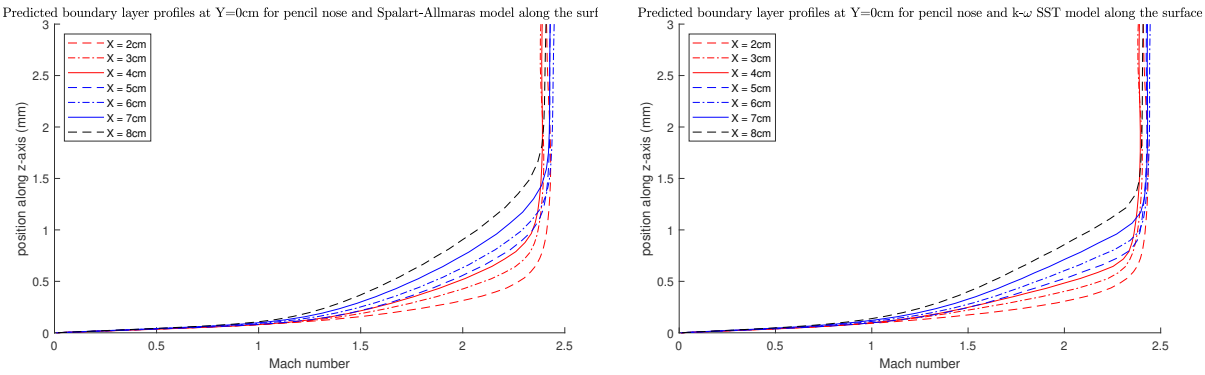

(a) Spalart-Allmaras turbulence model **(b) $k-\omega$ SST turbulence model**

Fig. 15 Boundary Layer Profiles along the body at the intersection of the lower face and symmetry plane for the pencil nose at Mach 2.5

Figures 16, 17a & 17b, obtained for the pyramidal nose shape, shows that the profiles converge to different Mach numbers depending whether they are located on the nose or the main body. This is a consequence of the body geometry as shown in Figure 13b. The geometry of the faces is similar to a corner followed by a flat plate. Since each geometrical change is followed by a constant, inclined or not, flat plate, the flow outside the boundary layer is kept constant until the next geometrical change. The increase in Mach number from the nose to the main body is due to the transition from an inclined surface to a zero-incidence flat plate which causes an expansion wave, thus reducing the density and increasing the Mach number.

Figures 18, 19 & 20, obtained for the tangent-ogive nose shape, shows the presence of the shock near the boundary layer at the nose limits the Mach number outside the boundary layer and the influence of the shock decreases with the distance of the shock from the surface. On the main body, the shock is far enough to have little or no influence on the boundary layer development.

The development of the boundary layer, which just has been presented for each nose shape, is consistent with the expected, and observed via Schlieren imaging technique, physics of the flow and its influence on the development of the boundary layer. These results, in addition to those presented in the previous subsection, prove the ability to capture, at least qualitatively, the overall flow physics for supersonic zero-incidence flows.

In the absence of experimental data to study the boundary layer, the predicted profiles are compared for the different turbulence model. If all the positions used in the previously introduced Figures have been considered, only the profiles located at 8 cm from the nose for conciseness, are shown in Figures 21, 22 & 23.

The boundary layer is predicted thicker by $k-\varepsilon$ Realizable model than by the other two. The difference between the profiles predicted by the Spalart-Allmaras model and by the $k-\omega$ SST model increases with the distance from the nose.

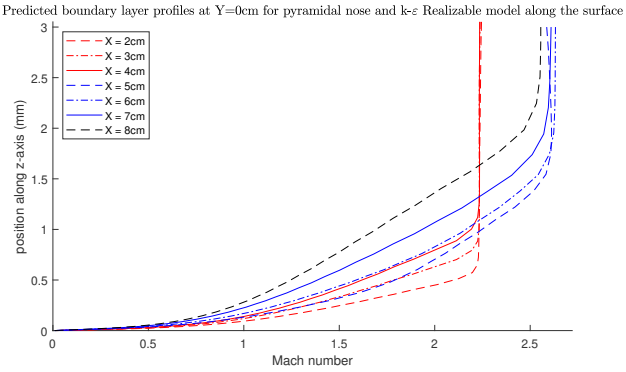

Fig. 16 Boundary Layer Profiles along the body at the intersection of the lower face and symmetry plane for the pyramidal nose and $k-\varepsilon$ Realizable turbulence model at Mach 2.5

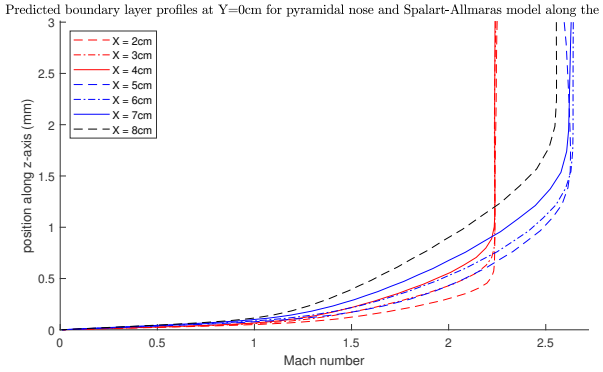

(a) Spalart-Allmaras turbulence model

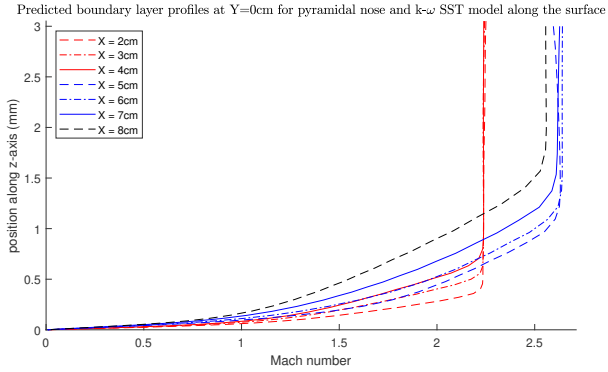

(b) $k-\omega$ SST turbulence model

Fig. 17 Boundary Layer Profiles along the body at the intersection of the lower face and symmetry plane for the pyramidal nose at Mach 2.5

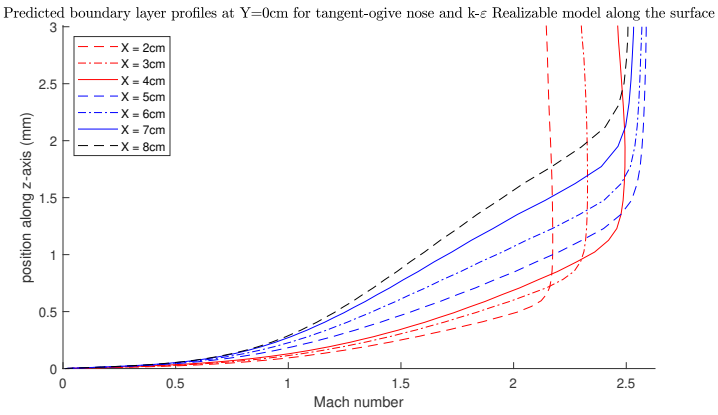

Fig. 18 Boundary Layer Profiles along the body at the intersection of the lower face and symmetry plane for the tangent-ogive nose and $k-\varepsilon$ Realizable turbulence model at Mach 2.5

The differences between turbulence models in predicting the boundary layer profile explain, at least partially, the results obtained in terms of forces. Since the predicted thickness of the boundary layer is higher for the $k-\varepsilon$ realizable model, the friction drag is more important due to a larger portion of the fluid involved in surface friction.

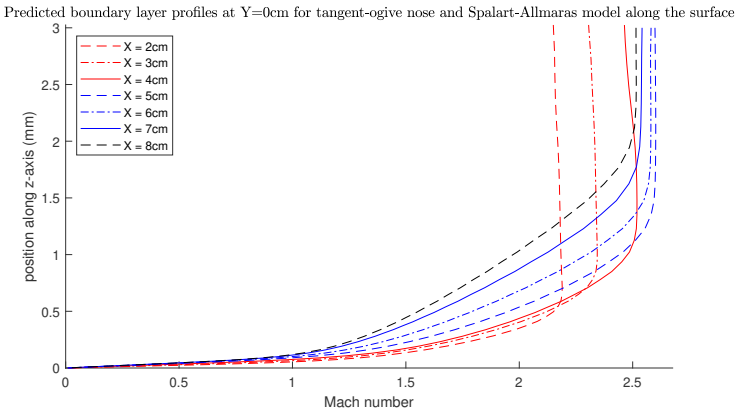

Fig. 19 Boundary Layer Profiles along the body at the intersection of the lower face and symmetry plane for the tangent-ogive nose and Spalart-Allmaras turbulence model at Mach 2.5

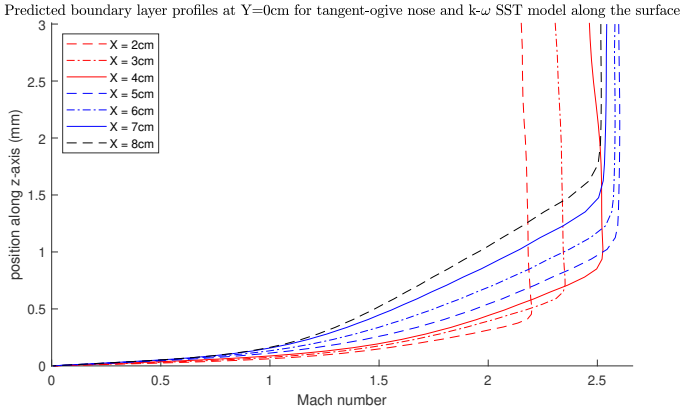

Fig. 20 Boundary Layer Profiles along the body at the intersection of the lower face and symmetry plane for the tangent-ogive nose and $k-\omega$ SST turbulence model at Mach 2.5

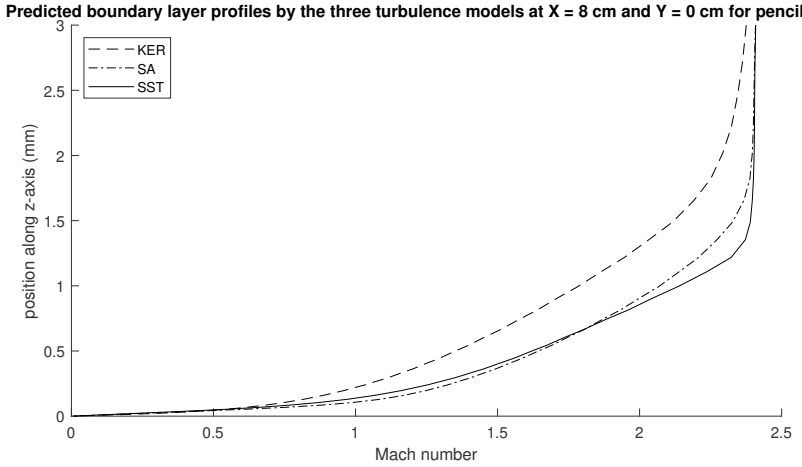

Fig. 21 Boundary layer profiles at 8 cm from the nose in the symmetry plane for the pencil nose depending the turbulence model, for the freestream Mach number is 2.5 & obtained on the lower face of the body

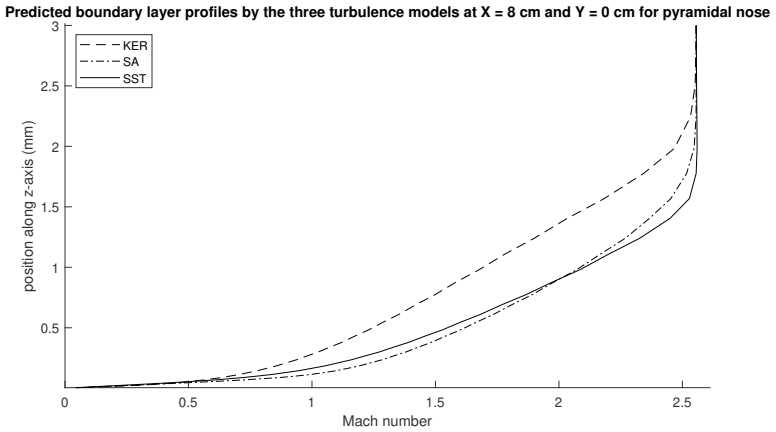

Fig. 22 Boundary layer profiles at 8 cm from the nose in the symmetry plane depending the turbulence model, for the pyramidal nose

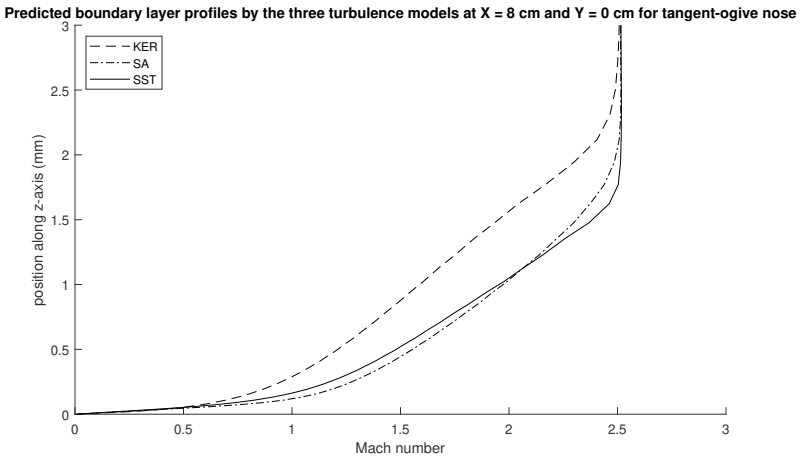

Fig. 23 Boundary layer profiles at 8 cm from the nose in the symmetry plane depending the turbulence model, for the tangent-ogive nose

B. Jorgensen Configuration

White-lead tests were performed at Mach 1.98 for 10° and 14° of angle of attack and at Mach 3.88 for 14° of angle of attack. The comparison of the white-lead tests with wall shear stress contours are shown in Figures 24 to 32.

The flow patterns observed are similar between the turbulence models. Overall, $k-\varepsilon$ Realizable model predicts higher values of wall shear stress than the other turbulence models. Spalart-Allmaras model predicts slightly superior wall shear stress than $k-\omega$ SST model. The position of the vortex is fairly accurately predicted by CFD, where the boundary layer detaches and consequently the wall shear stress is negligible at the vortex. This region appears in white due to the almost absence of friction to remove the white-lead solution. In CFD contours illustrated in figures presented in this Section, this region is shown in dark blue at Mach 1.98, and in blue at Mach 3.88.

In Figure 31, a region of low wall shear stress is predicted at the first half portion of the nose in the upper part of the side face. This region is observed with CFD and corresponds to a higher level of wall shear stress than the leeside vortex. This region is probably due to the interaction of the boundary layer with the vortex, which may create a gradient of pressure causing the local growth of the boundary layer. This phenomenon was investigated with the comparison between water vapour screens and total pressure contours in transverse planes.

Water-vapour screen images were obtained at two positions along the body: 5 and 10 reference lengths from the nose. These pictures are compared with total pressure contours in Figures 33 to 39. At Mach 1.98, images were acquired at the angles of attack: 5°, 10°, 14° and 17°. At Mach 3.88, images were acquired at the angles of attack: 5°, 10° and 14°.

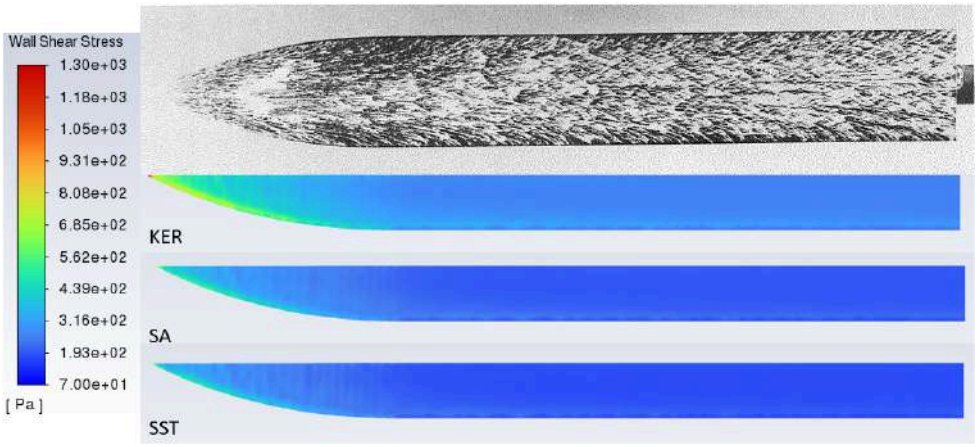

Fig. 24 Comparison of White-lead tests and shear stress contours at Mach 1.98 and an angle of attack of 10°, view of the model from the bottom

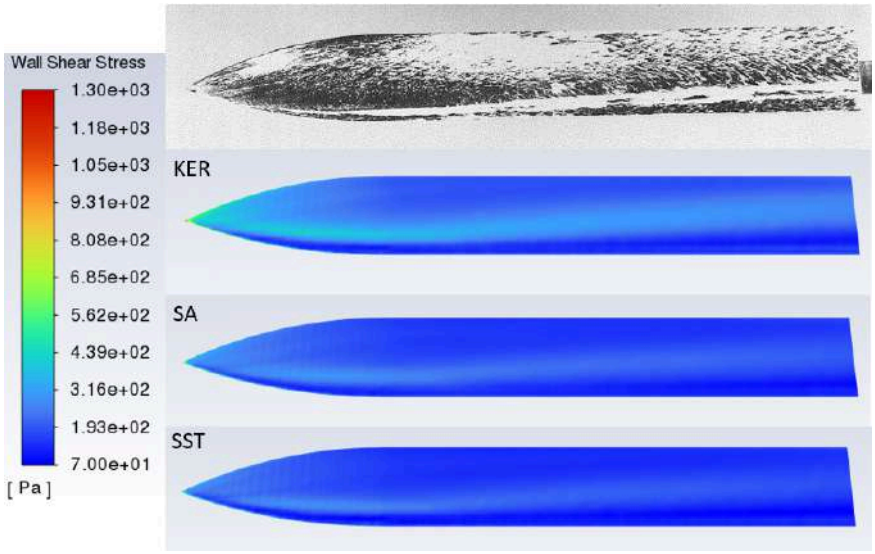

Fig. 25 Comparison of White-lead tests and shear stress contours at Mach 1.98 and an angle of attack of 10°, view of the model from the side

The body is 10 reference length long, thus the pictures for the screen at 5 reference length from the nose look like the vortex starts in the middle of the face. However, this look is due to the low contrast of the pictures and the depth effect. Actually, the vortex starts at the edge to form. The choice of total pressure for the contours was motivated to ensure an adapted color bar and scale for the reader but to still show the same pattern as Mach number or density contours would.

Overall, the vortex predicted with CFD has a similar shape and position as the pictures captured of the water-vapour screens. Due to the incidence of the body, the boundary layer separates near the lower edge of the face and the separated boundary layer starts to rotate. The vortex, thus formed, grows with the distance of the nose. The presence of the vortex modifies the pressure gradient on the faces and yields to thinner boundary layer on the inferior portion of the faces and thickened one near the upper edge. The influence of the vortex over the boundary layer is more important with larger and "stronger" vortices. By "stronger vortex", it means vortex where the minimal total pressure is smaller. The expansion, and the reduction, of the boundary layer respectively near the upper edge, and on the lower part of the face, disappear when the vortex is developed enough to interact with the boundary layer on the whole surface and when most of the boundary layer is separated as shown for instance in Figures 35b or 36b. This situation is observed at higher angles of attack. Increasing the incidence causes the formation of more spatially-extended vortices and lower total pressure in the core of the vortex. Increasing the Mach number limits to the ability of the vortex to develop far from the

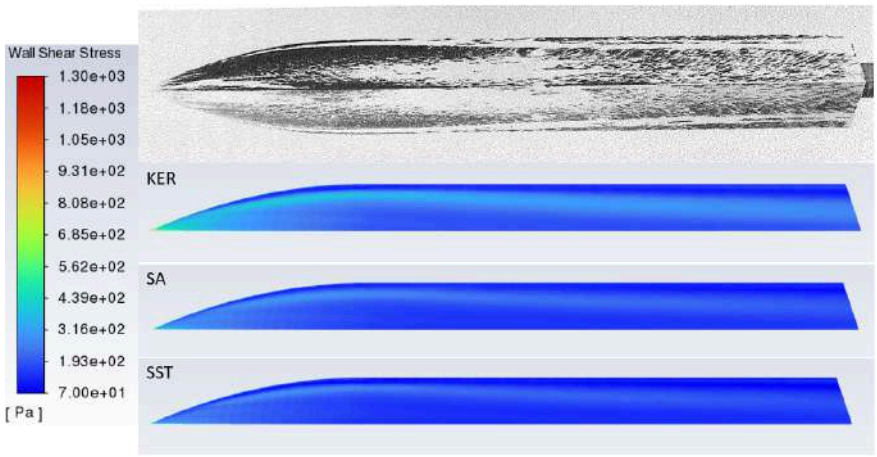

Fig. 26 Comparison of White-lead tests and shear stress contours at Mach 1.98 and an angle of attack of 10°, view of the model from the top

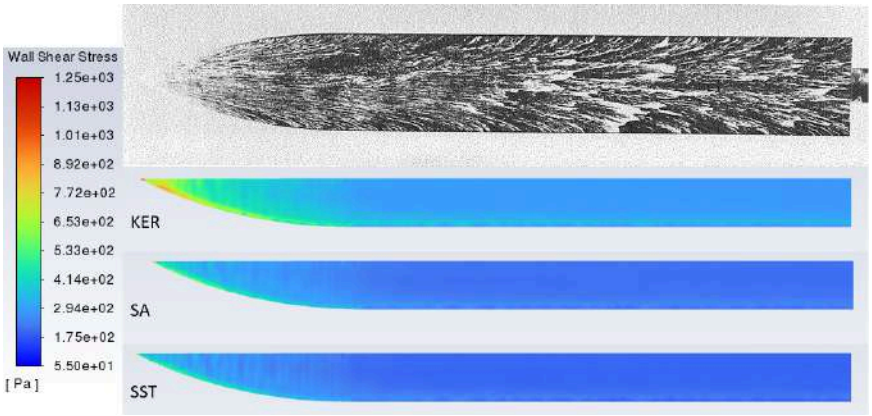

Fig. 27 Comparison of White-lead tests and shear stress contours at Mach 1.98 and an angle of attack of 14°, view of the model from the bottom

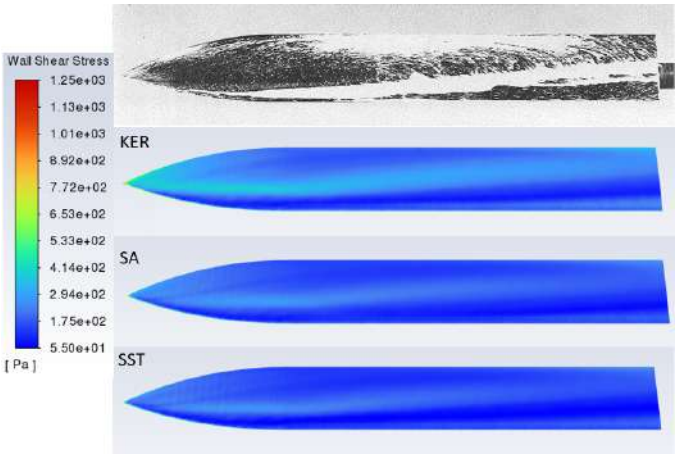

Fig. 28 Comparison of White-lead tests and shear stress contours at Mach 1.98 and an angle of attack of 14°, view of the model from the side

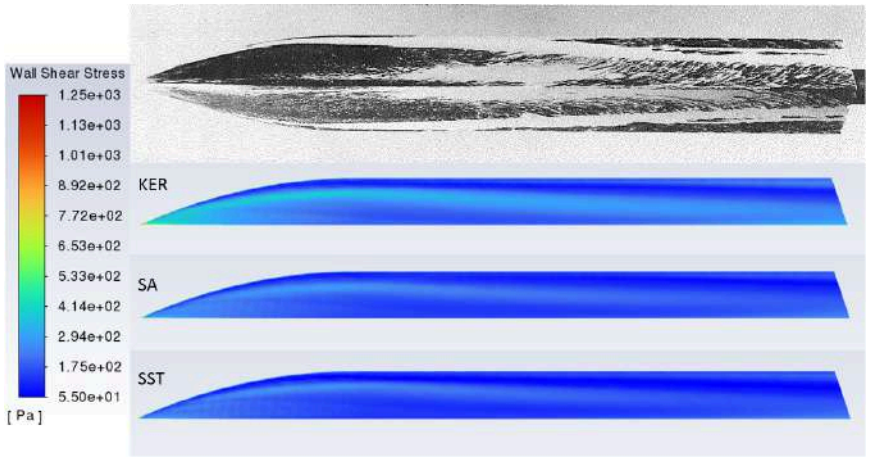

Fig. 29 Comparison of White-lead tests and shear stress contours at Mach 1.98 and an angle of attack of 14°, view of the model from the top

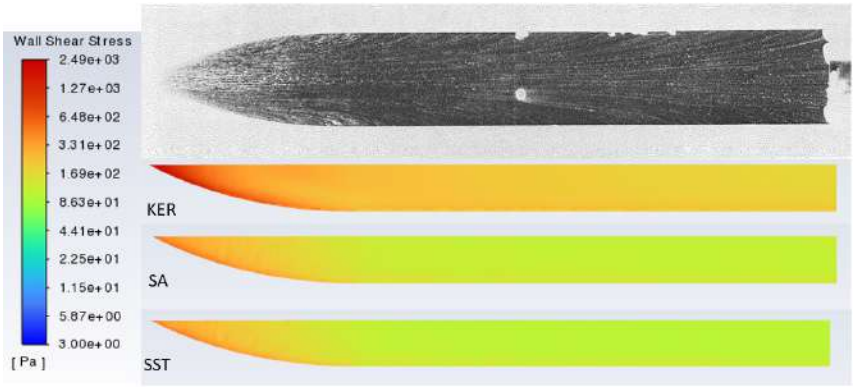

Fig. 30 Comparison of White-lead tests and shear stress contours at Mach 3.88 and an angle of attack of 14°, view of the model from the bottom

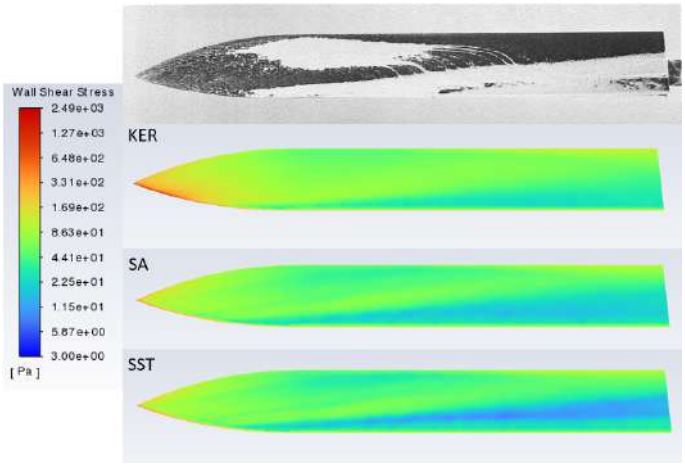

Fig. 31 Comparison of White-lead tests and shear stress contours at Mach 3.88 and an angle of attack of 14°, view of the model from the side

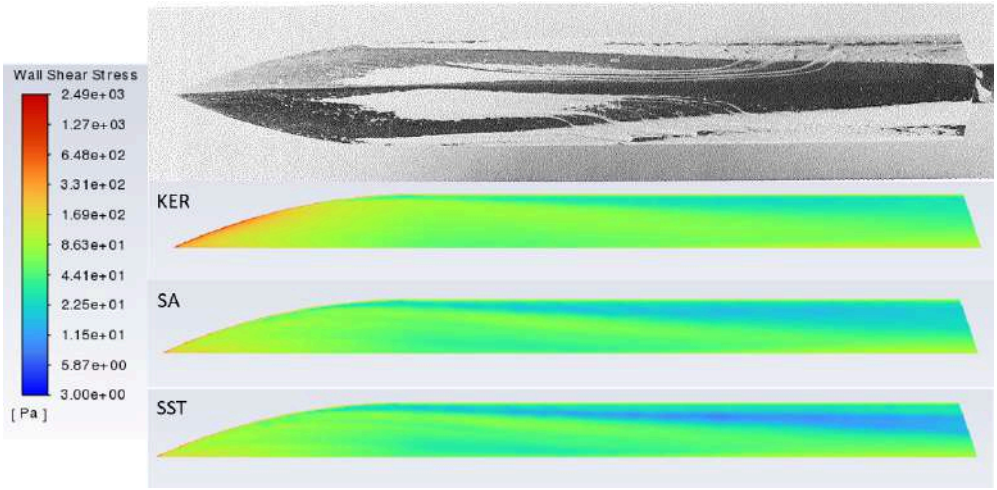

Fig. 32 Comparison of White-lead tests and shear stress contours at Mach 3.88 and an angle of attack of 14°, view of the model from the top

body and creates vortices almost stuck to the surface of body. This trend is clearly observed when comparing Figures for Mach 1.98 with these at Mach 3.88, especially at 14° of angle of attack.

Comparing the turbulence models, $k-\varepsilon$ Realizable model predicts larger zones of low total pressure and tends to smooth and average at higher angles of attack and higher Mach number the total pressure in and close to the vortex. This last statement is particularly clear in Figure 39b. $k-\omega$ SST model predictions are similar to Spalart-Allmaras model ones. Differences between the predictions of these two turbulence models arise at Mach 1.98 for the angles of attack 14° and 17° where the $k-\omega$ SST model gives larger detached regions with similar expansion as the predictions of $k-\varepsilon$ Realizable model.

The pictures of the water-vapour screens sometimes show the detached flow at the edge as in Figure 36a, but this technique is only qualitative giving the topology of the regions where the pressure is low enough to cause the condensation of the vapour. The agreement of the flow structures shown by this technique and the one predicted with CFD demonstrates the ability of the chosen turbulence models to investigate the flow topology for modest angles of attack, inferior to 17°, in supersonic regime.

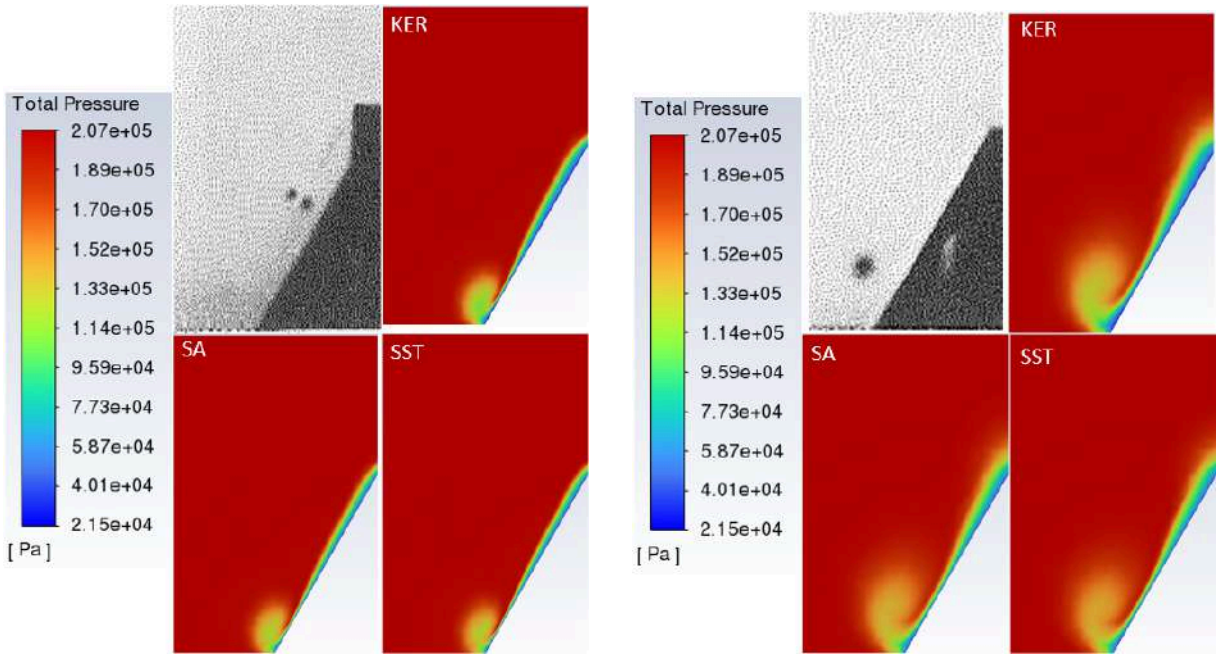

(a) at $x/L_{\text{ref}} = 5$ **(b) at $x/L_{\text{ref}} = 10$**

Fig. 33 Comparison of the water-vapour screen and the total pressure contours at Mach 1.98 and Angle of Attack 5°

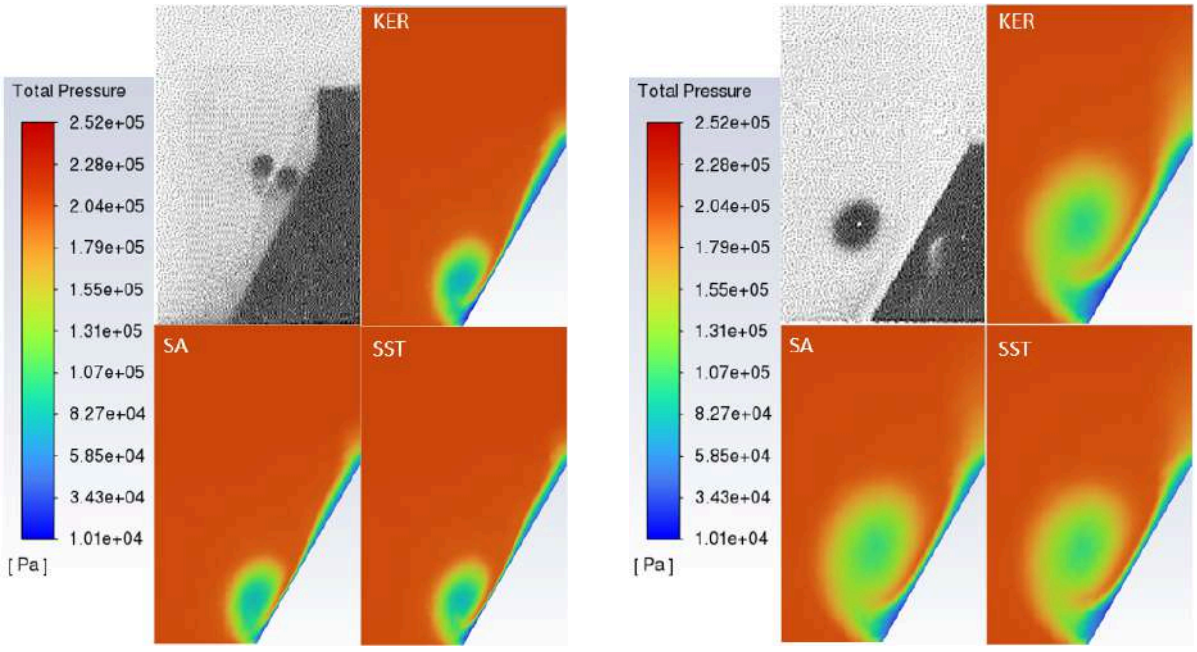

(a) at $x/L_{\text{ref}} = 5$ **(b) at $x/L_{\text{ref}} = 10$**

Fig. 34 Comparison of the water-vapour screen and the total pressure contours at Mach 1.98 and Angle of Attack 10°

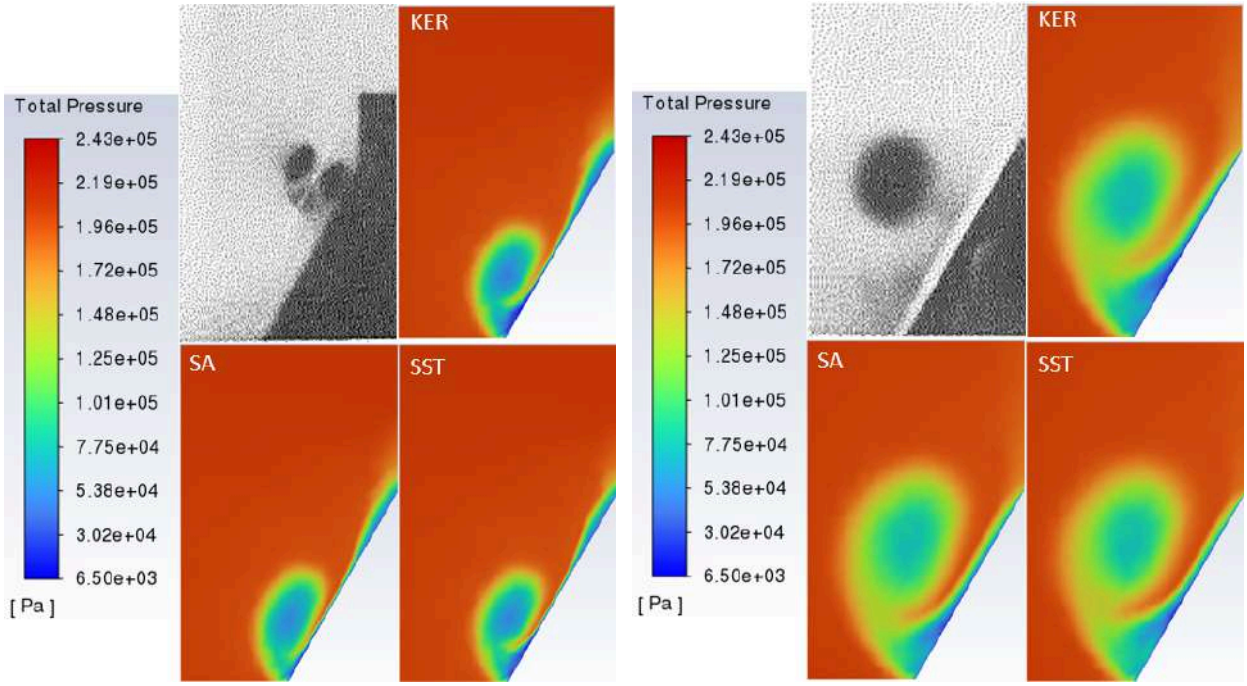

(a) at $x/L_{\text{ref}} = 5$ **(b) at $x/L_{\text{ref}} = 10$**

Fig. 35 Comparison of the water-vapour screen and the total pressure contours at Mach 1.98 and Angle of Attack 14°

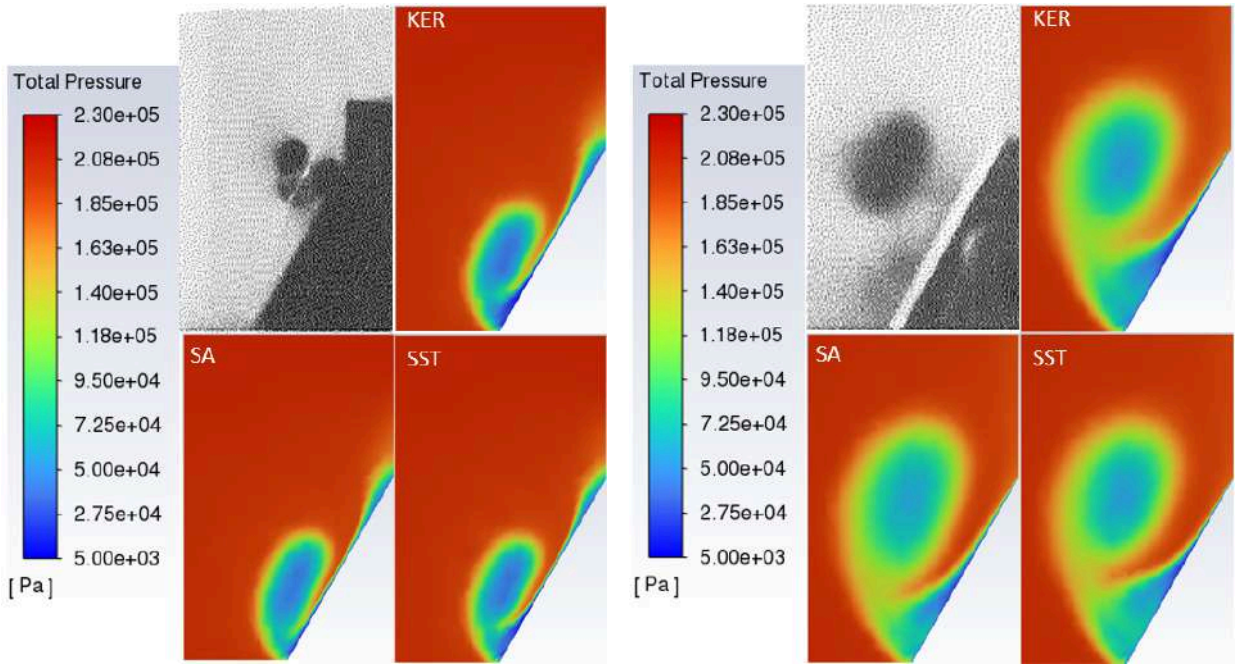

(a) at $x/L_{\text{ref}} = 5$ **(b) at $x/L_{\text{ref}} = 10$**

Fig. 36 Comparison of the water-vapour screen and the total pressure contours at Mach 1.98 and Angle of Attack 17°

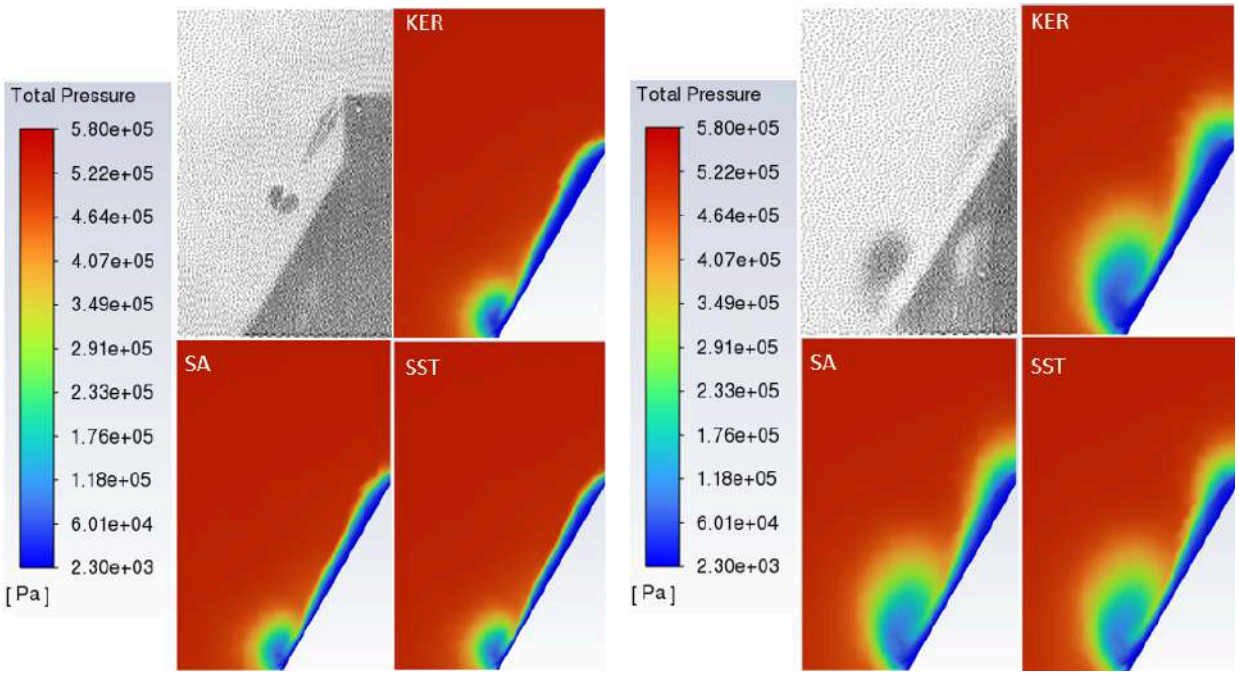

(a) at $x/L_{\text{ref}} = 5$ **(b) at $x/L_{\text{ref}} = 10$**

Fig. 37 Comparison of the water-vapour screen and the total pressure contours at Mach 3.88 and Angle of Attack 5°

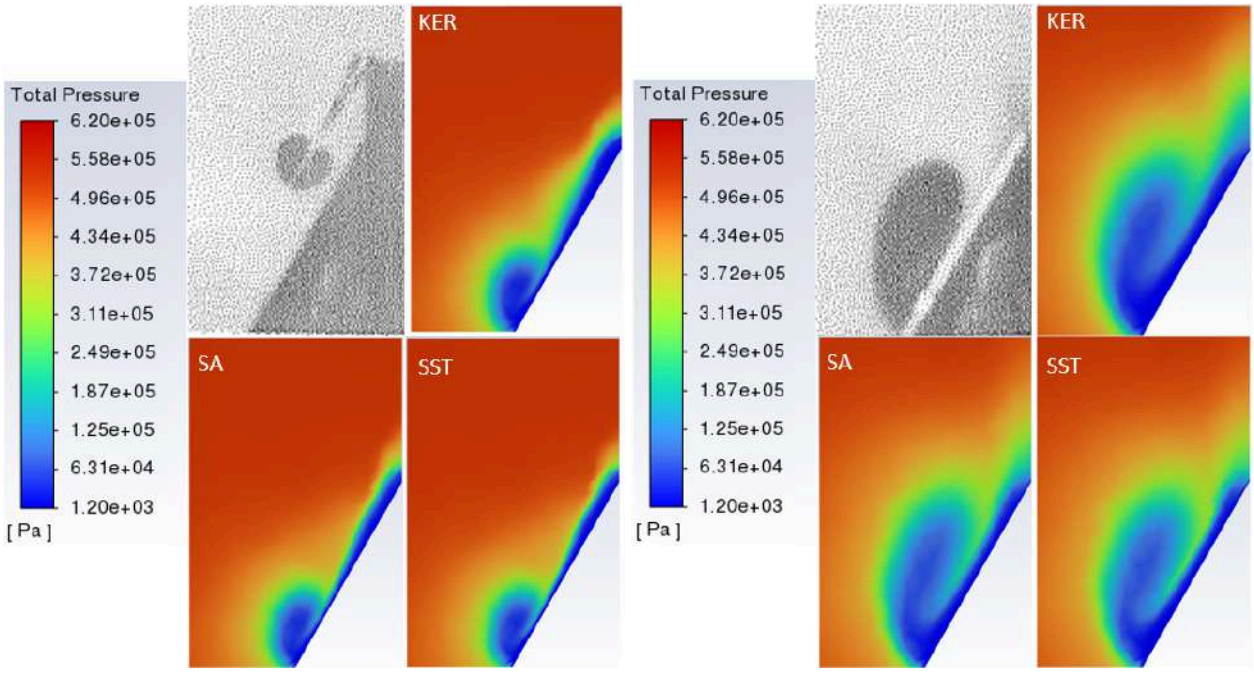

(a) at $x/L_{\text{ref}} = 5$ **(b) at $x/L_{\text{ref}} = 10$**

Fig. 38 Comparison of the water-vapour screen and the total pressure contours at Mach 3.88 and Angle of Attack 10°

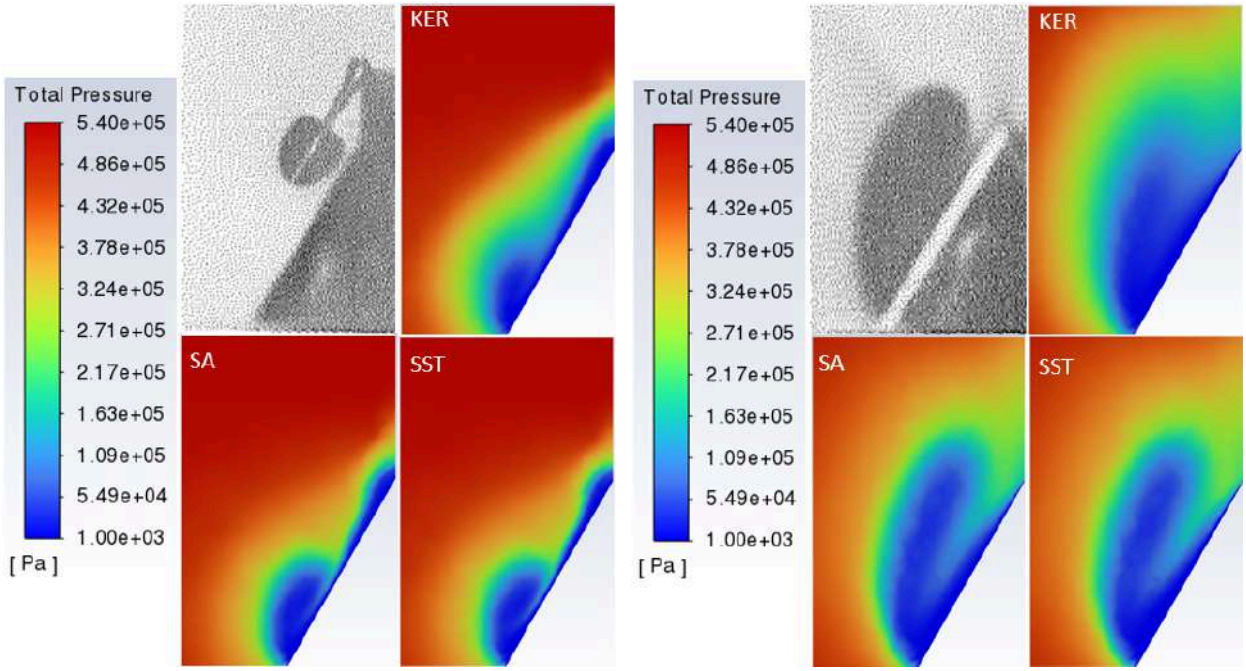

(a) at $x/L_{\text{ref}} = 5$ **(b) at** $x/L_{\text{ref}} = 10$

Fig. 39 Comparison of the water-vapour screen and the total pressure contours at Mach 3.88 and Angle of Attack 14°

V. Conclusion

The simulations showed an acceptable correspondence with flow features and measurements of the axial and normal forces. For the drag, Spalart-Allmaras and $k-\omega$ SST models gave similar values for most of the configurations while $k-\varepsilon$ Realizable model tends to predict superior value for the drag. For any nose shape, at Mach 2.5, the differences observed between the turbulence models in terms of drag are mainly due to the viscous drag, and thus to the development of the boundary layer along the body.

In terms of flow features, $k-\omega$ SST and Spalart-Allmaras models are superior to capture the leeside vortices, particularly at higher angles of attack. Considering the relatively similar results obtained with $k-\omega$ SST and Spalart-Allmaras models for most of the configurations, the use of $k-\omega$ SST which is more intensive in terms of computing resources and time than Spalart-Allmaras was not proved to have any significant interest, at least in the investigated configurations.

References

[1] Jorgensen, L. H., "Inclined bodies of various cross sections at supersonic speeds," Tech. rep., NASA, 1958.

[2] Carlson, H. W., and Gapcynski, J. P., "An experimental investigation at a Mach number of 2.01 of the effects of body cross-section shape on the aerodynamic characteristics of bodies and wing-body combinations," Tech. rep., NACA, 1955.

[3] Hutt, G. R., and Howe, A. J., "Effects of cross section and nose geometry on slender-body supersonic aerodynamics," *Journal of Spacecraft and Rockets*, Vol. 25, No. 2, 1988, pp. 189–192.

[4] Agrell, J., Hamner, O., and Jonsson, B., "Aerodynamic Characteristics of Missiles With Triangular Cross Sections," *21st Congress of International Council of the Aeronautical Sciences, Melbourne, Australia*, 1998, pp. 1–14.

[5] Morita, W., Yoneda, T., Aso, S., Tani, Y., and Inatani, Y., "Experimental Study on Effects of Fuselage Configurations for RLV on Aerodynamic Characteristics," *34th AIAA Fluid Dynamics Conference and Exhibit*, 2004.

[6] Prince, S., Caballero, R. G., and Pasquale, D. D., "Assessment of Turbulence Models for Transonic / Supersonic Smooth Surface Separation," 2021. https://doi.org/10.17862/cranfield.rd.14135261.v2, URL https://cord.cranfield.ac.uk/articles/preprint/Assessment_of_Turbulence_Models_for_Transonic_Supersonic_Smooth_Surface_Separation/14135261.

[7] Love, E. S., "The Base Pressure at Supersonic Speeds on Two-Dimensional Airfoils and Bodies of Revolution (With and Without Fins) Having Turbulent Boundary Layers," Naca research memorandum, National Advisory Committee for Aeronautics, 1953.

[8] Chapman, D. R., "An Analysis of Base Pressure at Supersonic Velocities and Comparison with Experiment," Naca technical report, National Advisory Committee for Aeronautics, 1950.

[9] Love, E. S., "A Summary of Information on Support Interference at Transonic and Supersonic Speeds," Naca research memorandum, National Advisory Committee for Aeronautics, 1954.

[10] Moore, F. G., Wilcox, F., and Hymer, T., "Improved Empirical Model for Base Drag Prediction on Missile Configurations Based on New Wind Tunnel Data," Report, Naval Surface Warfare Center, 1992.

[11] Sieling, W. R., and Page, R. H., "A Re-Examination of Sting Interference Effects," 1970.

[12] Uselton, B. L., and Haberman, D. R., "Summary of Sting Interference Effects for Cone, Missile and Aircraft Configurations as Determined by Dynamic and Static Measurements," 1982.

[13] Vos, R., and Farokhi, S., *Introduction to Transonic Aerodynamics*, Springer, 2015.

2023-06-08

Analysis of triangular cross-section slender bodies in supersonic regime using RANS simulations

Bourny, Quentin

AIAA

Bourny Q, Proença AR, Di Pasquale D, Prince SA. (2023) Analysis of triangular cross-section slender bodies in supersonic regime using RANS simulations. In: 2023 AIAA Aviation and Aeronautics Forum and Exposition (AIAA AVIATION Forum), 12-16 June 2023, San Diego, USA. Paper number AIAA 2023-4404

https://doi.org/10.2514/6.2023-4404